Computational Fluid Dynamic Modeling of a Baffled-Tube Ram Accelerator with Inclined Baffles

Jesse Dumas

A thesis submitted in partial fulfillment of the
requirements for the degree of

Master of Science in Aeronautics & Astronautics

University of Washington

2018

Committee:

Carl Knowlen, Chair

Robert Breidenthal

Program Authorized to Offer Degree:
Aeronautics & Astronautics

University of Washington

Abstract

Computational Fluid Dynamic Modeling of a Baffled-Tube Ram Accelerator with Inclined Baffles

Jesse Dumas

Chair of the Supervisory Committee:
Dr. Carl Knowlen
Aeronautics & Astronautics

The baffled-tube ram accelerator is a hypervelocity launcher device that accelerates a projectile through a stationary tube filled with a propellant mixture. In this work, to assist ongoing experimental research, a baffled-tube ram accelerator with baffles inclined toward the incoming projectile was simulated using unsteady computational fluid dynamic modeling to examine projectile and baffle drag forces as a function of projectile Mach number. Fourteen Mach numbers ranging from 0.95 to 4.32 were simulated solving both inviscid and turbulent flow equations in alternate cases, all in inert nitrogen. The recorded drag forces were used to calculate drag coefficients for the projectile and baffle walls, and these coefficients will be used to improve thermodynamic models to predict the thrust generated by the baffled-tube ram accelerator.

TABLE OF CONTENTS

LIST OF FIGURES

LIST OF TABLES

NOMENCLATURE

Greek Symbols

β geometric volume factor

γ ratio of specific heats at constant pressure per constant volume for a mixture

ϕ fuel equivalence ratio

ρ density

Initialisms

BTRA baffled tube ram accelerator

CFD computational fluid dynamics

SBRA smooth-bore ram accelerator

TCRA thermally choked ram accelerator

Symbols

a speed of sound

A_b bore area

A_{eff} effective area

C_d coefficient of drag

c_p specific heat at constant pressure

D	drag
d_b	bore diameter
d_c	chamber diameter
F	thrust
h	sensible enthalpy
I	non-dimensional thrust
L_c	chamber length
L_b	baffle length
M	Mach number
n_c	number of chambers
p	pressure
Q	non-dimensional heat release parameter
q	heat release per unit mass of propellant
R	gas constant
T	temperature
u	flow velocity
V_b	baffle volume
V_c	chamber volume

ACKNOWLEDGMENTS

I would like to express sincere appreciation to Carl Knowlen, Trevor Byrd, Navid Daneshvaran, John Hinkey, Jon Tonouchi, and the undergrads working in the ram lab, especially[1] Kristen Anderson, Conrad Blake, Andrew Hadford, Brandon Kawaguchi, Eric Kim, and Cole Morgan. Thanks[2].

[1] In alphabetical order.

[2] Sincerely.

DEDICATION

to Megan and Hoku

Chapter 1

INTRODUCTION

The smooth bore ram accelerator (SBRA) is a hypervelocity launcher device that accelerates a projectile, which is similar to the center body of a ramjet, through a stationary tube filled with a propellant mixture [1]. The device takes advantage of aerothermodynamic propulsive cycles that resemble those of a typical airbreathing ramjet engine [2], as shown in Figure 1.1, to accelerate projectiles from relatively low speeds up to roughly 3000 m/s. It has been proposed as a direct-to-orbit space launcher to compete with traditional chemical rockets since the SBRA projectiles do not need to carry their own propellants [3].

The operating limits of the SBRA have been researched at the University of Washington since 1983. One such limitation is the need for propellant mixture dilution to prevent the combustion-driven shock wave from jumping ahead of the projectile throat (see Figure 1.1), which leads to a 50-70% reduction in thrust compared to the theoretical maximum [4].

The baffled-tube ram accelerator (BTRA) is a concept intended to overcome performance limitations of the SBRA. The addition of baffles to a smooth bore creates annular chambers, and the projectile acts as a one way valve as it passes through, preventing shock waves from being forced ahead of the projectile. The process is pictured in Figure 1.2. This potentially allows the BTRA to deliver twice the thrust of the SBRA at the same propellant fill pressure [5].

Recent work has focused on developing theoretical predictions for BTRA performance similar to one-dimensional models that have been successful predicting SBRA thrust [6].

My thesis research characterized the performance of the BTRA through unsteady computational fluid dynamic (CFD) simulations. In particular, I have simulated several constant-speed projectiles moving through chambers with baffles angled toward the incoming projectile, while measuring drag on the projectile and baffle drag .

The intent of this research was to understand the operating envelope of the BTRA and to

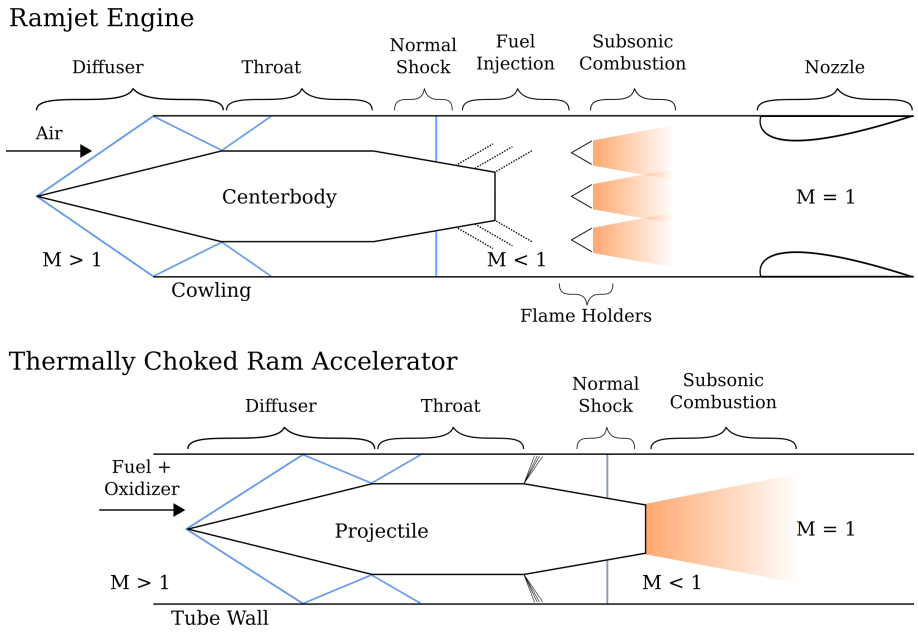

Figure 1.1: Ram accelerator similarities with ramjet engine.

supplement and support the development of theoretical models for the BTRA, and it builds on previous CFD performed by my peers [7, 8, 9]. I calculated projectile and baffle drag coefficients that will be used to refine one-dimensional thermodynamic models predicting thrust in the BTRA. Additionally, my work can be used as an engineering tool to improve similar calculations in the future.

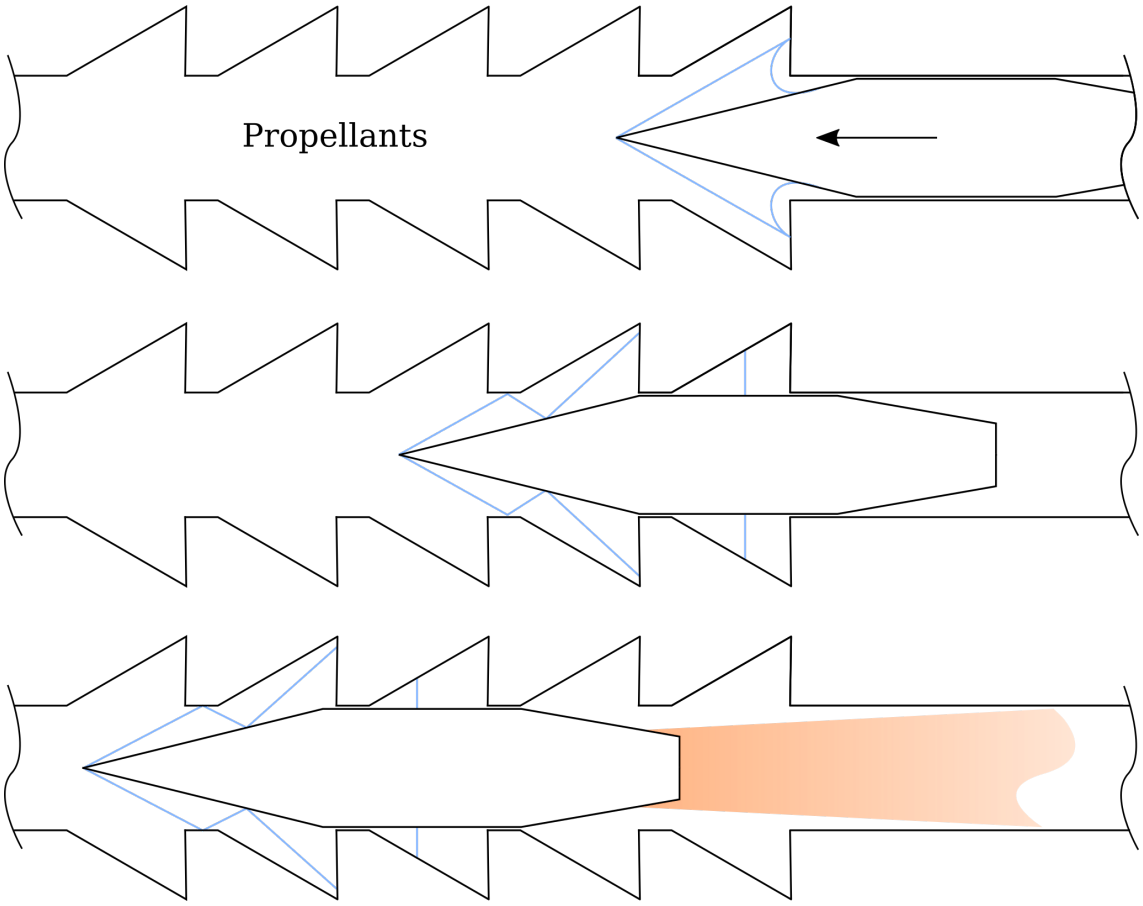

Figure 1.2: A simplified diagram of the baffled-tube ram accelerator operating principles. Note: Actual shock patterns and interactions are more complex. **Top:** The projectile enters the baffled section and generates conical shock waves. **Middle:** Propellants are compressed and heated by normal shock waves. **Bottom:** The projectile base acts as a bluff body and stabilizes subsonic combustion, increasing pressure and accelerating the projectile.

Chapter 2

THEORY

Like the SBRA, the BTRA operates in a thermally choked propulsive mode. The thermally choked ram accelerator (TCRA) is analyzed using one-dimensional quasi-steady and unsteady models by applying gas dynamic conservation equations for energy and momentum.

2.1 Zero-Dimensional Thrust Model

Flow in the full tube area behind the projectile is steady and thermally choked. The flow conditions upstream of the projectile uniquely determine the heat release from combustion and the thrust on the projectile, independent of the flow field around the projectile. This model accurately predicts acceleration for velocities ≤ 0.9 CJ speed, but it cannot predict successful acceleration—that requires details of the flow field [4].

2.2 One-Dimensional Thrust Model

2.2.1 Overview of TCRA Concept

Under the assumption that the flow in the TCRA is 1-D and quasi-steady, the flow conditions upstream of the projectile and at the thermally choked plane describe the ram accelerator thrust [1]. Figure 2.1 illustrates the control volume.

The flow entering the control volume at station 1 is assumed to be isentropic, save for one normal shock on the body of the projectile. In reality, the single shock is replaced by a train of oblique shocks. Rayleigh flow, constant heat addition, is assumed behind the projectile.

This model of the flow field imposes three conditions [4]. First, there is a minimum Mach number keeping the flow supersonic past the projectile throat, preventing an unstart. Second, there is a maximum heat addition, Q_{max}, beyond which unstart occurs. Finally,

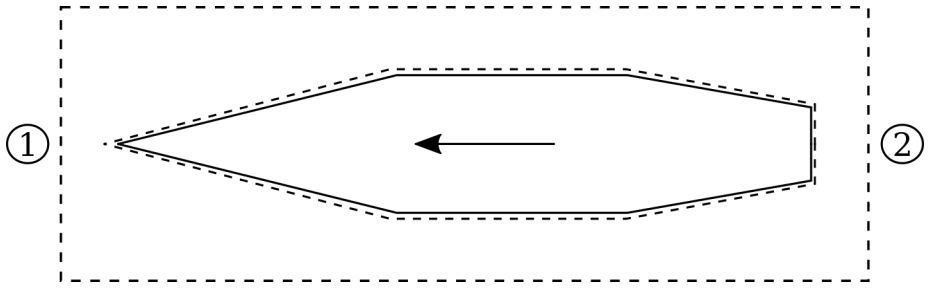

Figure 2.1: Ram accelerator control volume.

the shock will fall off the projectile base unless a minimum heat addition, Q_{min}, is met.

2.2.2 Applying the Theory to the SBRA

Describing the operation of the SBRA begins with the conservation equations and follows the method found in [1, 4, 10, 7]. Applying conservation of mass around the projectile ensures that the mass entering and leaving the control volume are the same:

$$\rho_1 A_1 u_1 = \rho_2 A_2 u_2 \tag{2.1}$$

Next, by conservation of momentum, the static pressure and momentum flux in and out of the control volume must be equal to the force applied to the projectile:

$$P_1 A_1 + \rho_1 A_1 u_1^2 + F = P_2 A_2 + \rho_2 A_2 u_2^2 \tag{2.2}$$

Conservation of energy stipulates that the energy flux leaving the control volume equals the energy flux in plus the heat release from chemical reactions, Δq,

$$h_1 + \frac{1}{2}u_1^2 + \Delta q = h_2 + \frac{1}{2}u_2^2\,, \tag{2.3}$$

where $h = h(T)$ is the sensible enthalpy for a calorically perfect gas.

The ideal gas law provides an equation of state:

$$P = \rho R T\,. \tag{2.4}$$

With the speed of sound,

$$a = \sqrt{\gamma RT}\,, \tag{2.5}$$

we can establish the Mach number,

$$M = \frac{u}{a}\,. \tag{2.6}$$

Next, we rewrite conservation of momentum in terms of pressure ratio, $\frac{P_2}{P_1}$, density ratio $\frac{\rho_2}{\rho_1}$, and non-dimensional thrust, $\frac{F}{P_1 A}$:

$$1 + M_1^2 a_1^2 \frac{\rho_1}{P_1} + \frac{F}{P_1 A} = M_2^2 a_2^2 \frac{\rho_2}{P_2} + \frac{P_2}{P_1}\,. \tag{2.7}$$

$$\frac{P_2}{P_1} = \frac{M_1}{M_2}\sqrt{\frac{\gamma_1 R_2 T_2}{\gamma_2 R_1 T_1}}\,. \tag{2.8}$$

It is helpful to define the one-dimensional heat release:

$$Q \equiv \frac{\Delta q}{c_{p1} T_1}\,. \tag{2.9}$$

Then, rewrite conservation of energy in terms of static temperature ratio, $\frac{T_2}{T_1}$, constant pressure heat capacity ratio, $\frac{c_{p1}}{c_{p2}}$, and non-dimensional enthalpy $\frac{h_1}{c_{p1} T_1}$:

$$\frac{h_1}{c_{p1} T_1} + \frac{\gamma_1 - 1}{2} M_1^2 + Q = \frac{h_2}{c_{p2} T_2} + \frac{\gamma_2 - 1}{2} M_2^2 \frac{c_{p2} T_2}{c_{p1} T_1}\,, \tag{2.10}$$

where

$$\frac{T_2}{T_1} = \frac{c_{p1}}{c_{p2}} \left(\frac{\frac{h_1}{c_{p1} T_1} + \frac{\gamma_1 - 1}{2} M_1^2 + Q}{\frac{h_2}{c_{p2} T_2} + \frac{\gamma_2 - 1}{2} M_2^2} \right). \tag{2.11}$$

Combining the previous relationships, we arrive at the non-dimensional thrust for the SBRA:

$$I_{SBRA} = \frac{F}{P_1 A} = \frac{M_1 \gamma_1}{M_2 \gamma_2} (1 + \gamma_2 M_2^2) \sqrt{\frac{\gamma_2 - 1}{\gamma_1 - 1} \left(\frac{\frac{h_1}{c_{p1} T_1} + \frac{\gamma_1 - 1}{2} M_1^2 + Q}{\frac{h_2}{c_{p1} T_1} + \frac{\gamma_2 - 1}{2} M_2^2} \right)} - (1 + \gamma_1 M_2^2)\,. \tag{2.12}$$

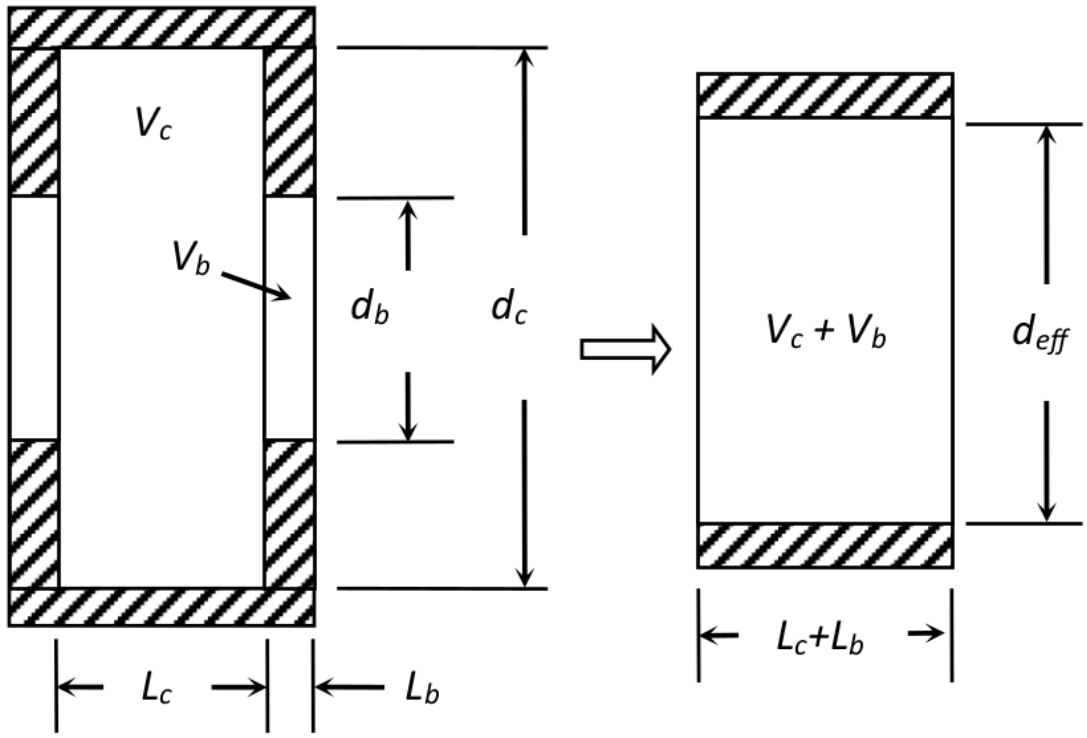

Figure 2.2: Baffle dimensions.

To relate I_{SBRA} to I_{BTRA}, a geometrical constant, β, is constructed from chamber-to-projectile diameter ratio, $\frac{d_c}{d_p}$, baffle thickness, t_b, chamber width, w_c, chamber volume, V_C, and baffle volume, V_b, to equate BTRA chamber volume to SBRA chamber volume with an effective bore diameter, d_{eff}, shown in Figure 2.2 [5].

$$\beta = \frac{1 + \left(\frac{w_c}{t_b}\right)}{1 + \left(\frac{w_c}{t_b}\right)\left(\frac{d_c}{d_p}\right)^2} \tag{2.13}$$

This relates non-dimensional, quasi-steady thrust of the SBRA to the BTRA.

$$I_{BTRA} = \frac{I_{SBRA}}{\beta}\,. \tag{2.14}$$

Baffle drag, D, is the lost momentum of gases moving through the baffles that would otherwise accelerate the projectile, and it must be included for a complete picture of forces acting in the control volume.

It is most convenient to simply subtract the impact of baffle drag from the previously derived conservation equations for momentum and energy:

$$P_1 A_1 + \rho_1 A_1 u_1^2 + F + D = P_2 A_2 + \rho_2 A_2 u_2^2 \tag{2.15}$$

$$\rho_1 A_1 u_1 (h_1 + \frac{1}{2}u_1^2 + \Delta q) - D u_1 = \rho_2 A_2 u_2 (h_2 + \frac{1}{2}u_2^2)\,. \tag{2.16}$$

Now, the finished expression for non-dimensional thrust in the BTRA is:

$$\begin{aligned} I_{BTRA} = {} & \frac{M_1 \gamma_1}{2}(1+\gamma_2)\sqrt{\left(\frac{\gamma_2 - 1}{\gamma_1 - 1}\right)\left(\frac{\frac{h_1}{c_{P1}T_1} + \frac{\gamma_1 - 1}{2}M_1^2 + Q - \frac{D(\gamma_1 - 1)}{P_1 A_1 \gamma_1}}{\frac{h_2}{c_{P1}T_1} + \frac{\gamma_2 - 1}{2}}\right)} \\ & - (1 + \gamma_1 M_1^2) - \frac{D}{P_1 A_1}\,. \end{aligned} \tag{2.17}$$

The drag term here is the baffle drag, defined as

$$D = C_d \rho_1 A_{p,b} n_c |u_1 - u_2|(u_1 - u_2)\,, \tag{2.18}$$

where $A_{p,b}$ is the projected area of the baffles, normal to the flow, and n_c is the number of chambers effected by high pressure drag. In this study, $n_c = 6$, as suggested by Daneshvaran [7], though the value is highly dependent on projectile and baffled-tube geometry.

Chapter 3

EXPERIMENTAL APPARATUS AND DEVELOPMENT AND IMPLEMENTATION OF CFD MODELS

3.1 The Experiment

The ram accelerator laboratory at the University of Washington has a 16 m test section with a 38-mm-bore diameter. The test section is preceded by a light gas gun providing initial projectile acceleration to entrance velocities as high as 1200 m/s. A muzzle gas dump tank and projectile catcher tube follow the test section. The test section contains a high pressure portion–which includes the 2 m baffled-tube test section–and a subsequent lower pressure portion [11]. Pressure is measured by piezoelectric pressure transducers (PCB119), and electromagnetic (EM) coil sensors designed at the University of Washington gather time-of-flight data, though BTRA entrance and exit velocities are used to find the average speed of the projectile passing through the baffled section due to signal distortion from the baffle geometry [9].

During tests[1], the baffled-tube segment is separated by thin Mylar diaphragms[2] from the rest of the apparatus, which is evacuated by vacuum pumps, and filled with propellant mixtures to pressures ranging from 1.0 MPa to 2.7 MPa for recent testing (up to a maximum 5 MPa for the apparatus) [9].

I have compared my nonreacting simulations to a shot in inert N_2, designated Cold Shot 96 (CS96). CS96 was performed with inward facing, angled baffles at a fill pressure of 1.1 MPa. Figures 3.1 and 3.3 show dimensions for the baffle inserts and projectile, respectively.

---

[1]Shots, as they're known

[2]Easily punctured by the incoming projectile.

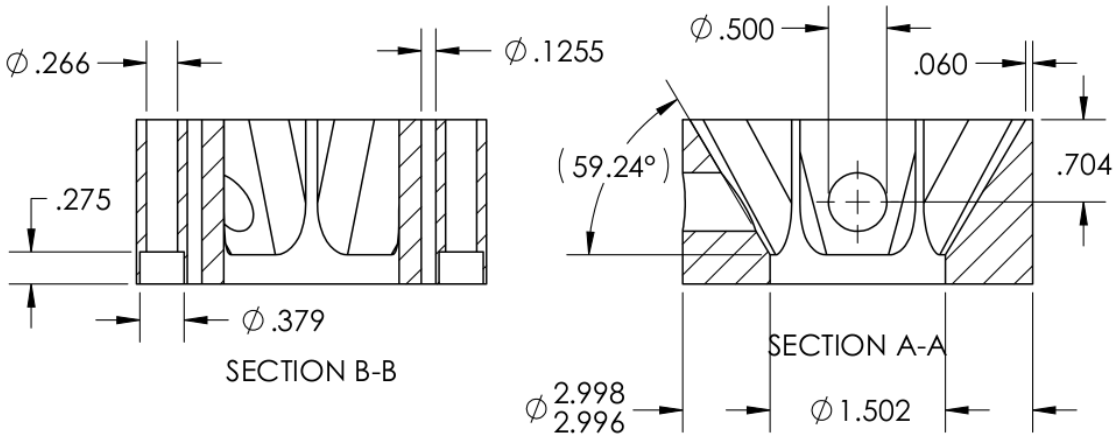

Figure 3.1: Engineering drawing of 30.8° baffle inserts with dimensions in inches.

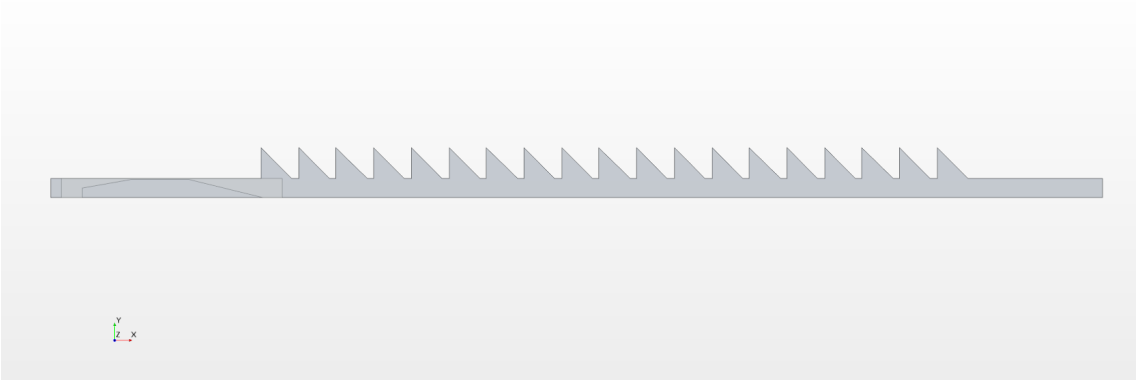

Figure 3.2: The axisymmetric baffled-tube computational geometry.

3.2 Computational Domain

3.2.1 Baffled-Tube Geometry

The baffled section of the domain, sized to match the geometry of recent experiments [6], contained 19 baffles inclined at 45° and angled toward the incoming projectile. Each individual baffle section was 29 mm long and had a 7 mm section of smooth-bore tube with a diameter of 38 mm. This simplified geometry is shown in Figure 3.2.

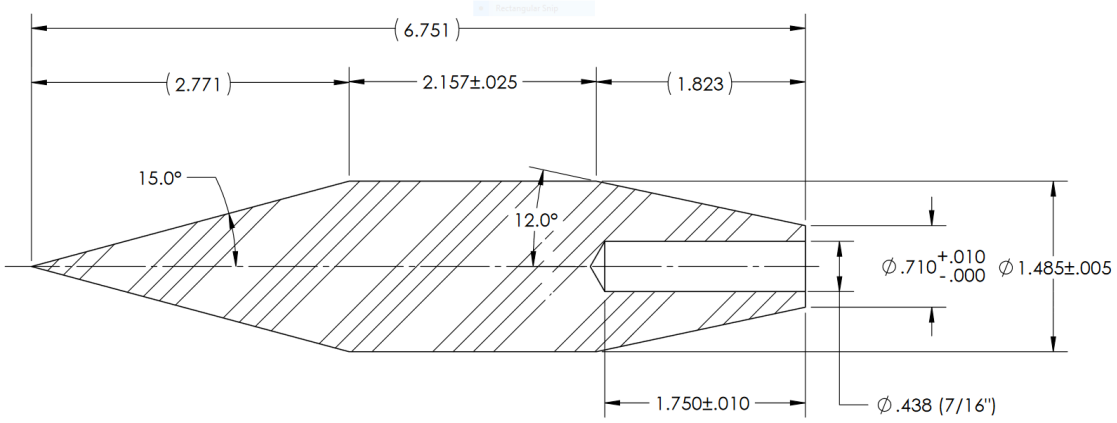

Figure 3.3: Projectile drawing with dimensions in inches.

3.2.2 Baffled-Tube Boundary Conditions

The baffle walls were given no-slip boundary conditions with zero surface roughness. The tube inlet and outlet were set as pressure outlet boundaries (Dirichlet boundary conditions) with a boundary value of 5 atm to prevent sudden outflow from the high pressure test section. The centerline of the baffled tube had an axis boundary condition.

3.2.3 Projectile Geometry

A 171 mm long axisymmetric projectile with a 15° nose cone was simulated. The 37.7 mm diameter shoulder connected to a 12° boat tail angle which tapered to an 18 mm diameter bluff base, shown in Figure 3.3. Note that the simulated projectile, Figure 3.4, had a solid base, as would the physical projectile after being instrumented with a magnet for time of flight measurements.

3.2.4 Projectile Boundary Conditions

The nose, body, tail, and base of the projectile had no slip wall boundaries with surface roughness set to zero. The centerline was an axis boundary. The region also contained overset interface boundaries forming a box (with the axis) around the projectile. This

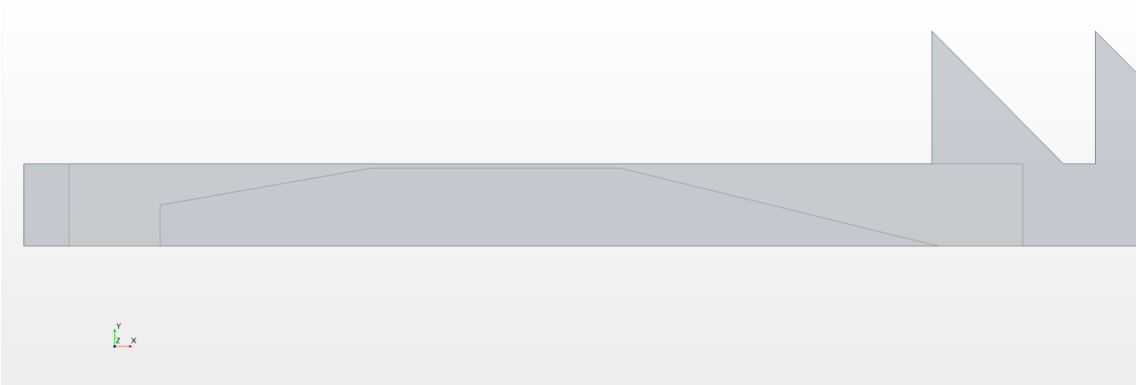

Figure 3.4: The axisymmetric projectile computational geometry.

permitted STAR-CCM+ to pass information between the moving projectile region and the stationary baffled-tube region.

3.2.5 Moving Region

The moving overset region containing the projectile, Figure 3.4, was given a constant velocity in the positive x-direction. Translation in the y-direction and rotation were note allowed, and the lack of any fluid-solid interaction model meant that the projectile would not react to any forces exerted by the fluid.

3.3 Flow Solver

3.3.1 Unsteady Solution

To run this transient analysis, an implicit unsteady solver was used to model the coupled flow, meaning the conservation equations for mass, momentum, and energy were solved simultaneously using a pseudo-time-marching approach [12]. First order temporal discretization was used with an initial time step of 10^{-6} s, and the time step was allowed to vary to keep the convective Courant number[3], C_{conv}, between 0.5 and 50.

[3]Also known as the Courant-Friedrichs-Lewy (CFL) condition.

3.3.2 Turbulence

Inviscid

The majority of the simulations run were inviscid and did not model the effects of turbulence. This is justified for supersonic flows since the drag is dominated by wave drag (pressure forces), and the impact of viscous shear forces contributes on the order of 5% of the total drag [13].

k-ω SST Model

To verify the assertion that inviscid modeling would provide sufficiently accurate drag force predictions, six simulations were run with the k-ω SST two-equation turbulence model. The model was chosen for its "popularity" and insensitivity to freestream values of model variables [14].

3.4 Meshing Strategy

3.4.1 General Settings

A polygonal mesher was used with a base size of 0.5 mm, which is shown in Figure 3.5. The projectile region contained 14,521 cells, and the tube region had 184,543, for a total of 199,064 cells. To capture boundary layer effects near the tube and projectile walls, a prism layer was used. The prism layer, pictured in Figure 3.6, had a total thickness of 33.3% of the base size (0.167 mm), and a stretching factor of 1.2 took the 15 prism cells from a thickness of 2.25×10^{-6} m to 3.0×10^{-5} m.

3.4.2 Overset Mesh

The mesh in the moving region was handled by using an overset, or "chimera," mesh. The overset mesh discretized the computational domain into a background and overset region. The separate, overlapping meshes included cells grouped into active, inactive, donor, and acceptor cells. Cells in the moving overset region were given highest priority over any cells they overlap in the background region and were always active [12]. Cells in the background

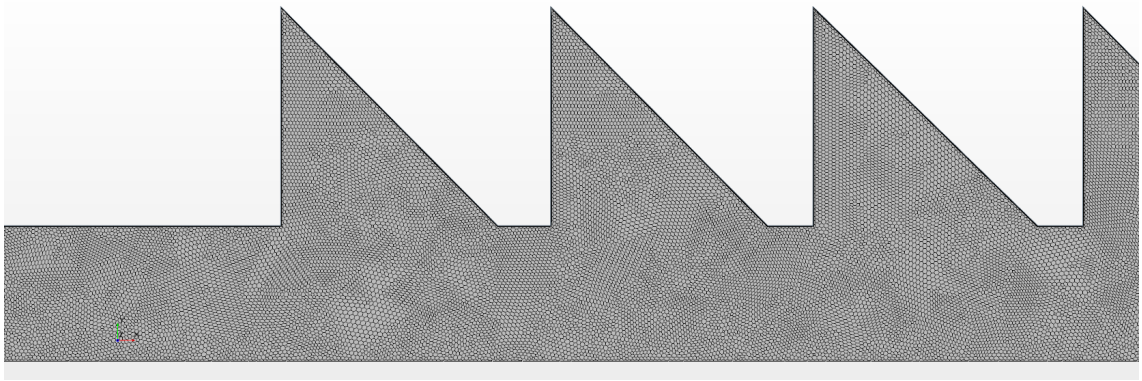

Figure 3.5: The axisymmetric, polygonal mesh with a base size of 0.5 mm.

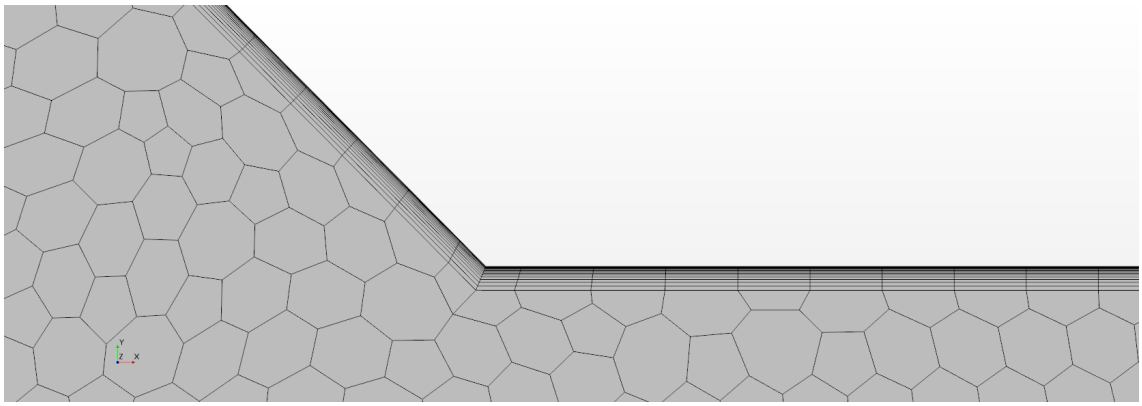

Figure 3.6: A prism layer made of 15 cells, implemented to capture boundary layer effects.

mesh behind the overset region were inactive, and cells at the boundary of the overset region were acceptor cells. Active cells at the overset boundary of the background region were active donor cells. The governing equations were solved on active cells, and variable values in acceptor cells were interpolated from donor cells. The overset and background meshes were implicitly coupled, and the solution was computed simultaneously in all active cells.

3.5 Initial Conditions

Simulations were run at Mach numbers ranging from $M = 0.95$ to $M = 4.32$. Table 3.1[4] shows which Mach numbers were simulated by case. The initial pressure for all simulations was set to 5 atm, and the initial static temperature was 300 K. The initial velocity in the domain was 0.0 m/s.

[4]Case 15 failed to converge.

Table 3.1: Projectile velocity, Mach number, and turbulence model by case.

Case	u	M	Turbulent/Inviscid
1	330	0.95	Inviscid
2	400	1.15	Inviscid
3	500	1.44	Inviscid
4	600	1.73	Inviscid
5	700	2.02	Inviscid
6	800	2.30	Inviscid
7	900	2.59	Inviscid
8	1000	2.88	Inviscid
9	1300	3.74	Inviscid
10	1400	4.03	Inviscid
11	1500	4.32	Inviscid
12	850	2.45	Turbulent
13	1200	3.46	Turbulent
14	900	2.59	Turbulent
16	425	1.22	Turbulent
17	1500	4.32	Turbulent

Chapter 4

RESULTS AND DISCUSSION

4.1 Drag Coefficient vs. Mach Number

4.1.1 Projectile Drag

In every simulation, the drag forces (F_d) were recorded; for the inviscid cases, this was the integral of the pressure forces over the projectile surface, and the turbulent cases also accounted for shear forces. The drag coefficient (C_d) was calculated using

$$C_d = \frac{2F_d}{\rho u^2 A}\,, \tag{4.1}$$

where $\rho = 7.06$ kg/m is the free stream density (at 5 atm), u is the free stream velocity, and A is the area of the projectile normal to the direction of movement. Both F_d and A were multiplied by 2π (since the quantities were recorded on a per radian basis for the axisymmetric simulations), but this amounts to multiplying the fraction by 1.

Figure 4.1 shows the cyclical behavior of C_d as the projectile travels through the baffled section. Though drag data were recorded during the entire simulation, I am focusing only on data gathered when the entire projectile moved through the baffled section; transients as the projectile entered and exited the baffled section are omitted for this study, but the full data are available (see Appendix A). The measurement accounts for drag over the entire projectile and is plotted against the position of the projectile base, so there is a phase shift in peak drag. The maximum drag occurs when the shoulder of the projectile (which is 101 mm ahead of the base) passes the entrance or exit of each chamber. The double peaks (note the low and high peaks in Figure 4.4) in C_d coincide with the projectile shoulder passing the straight, horizontal section of each baffle, which was 7 mm long.

Figure 4.2 shows C_d as the projectile passed through one chamber to the next. The average C_d was around 0.27, and the minimum maximum were about 40% below and above

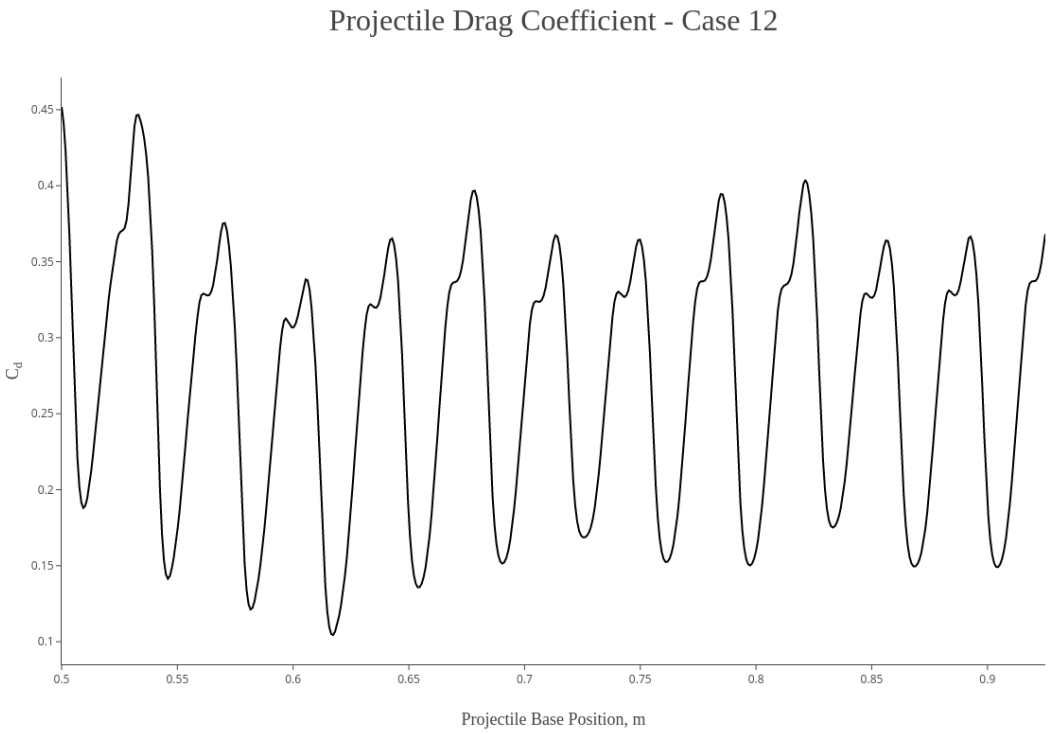

Figure 4.1: The drag coefficient as the projectile moves through the BTRA.

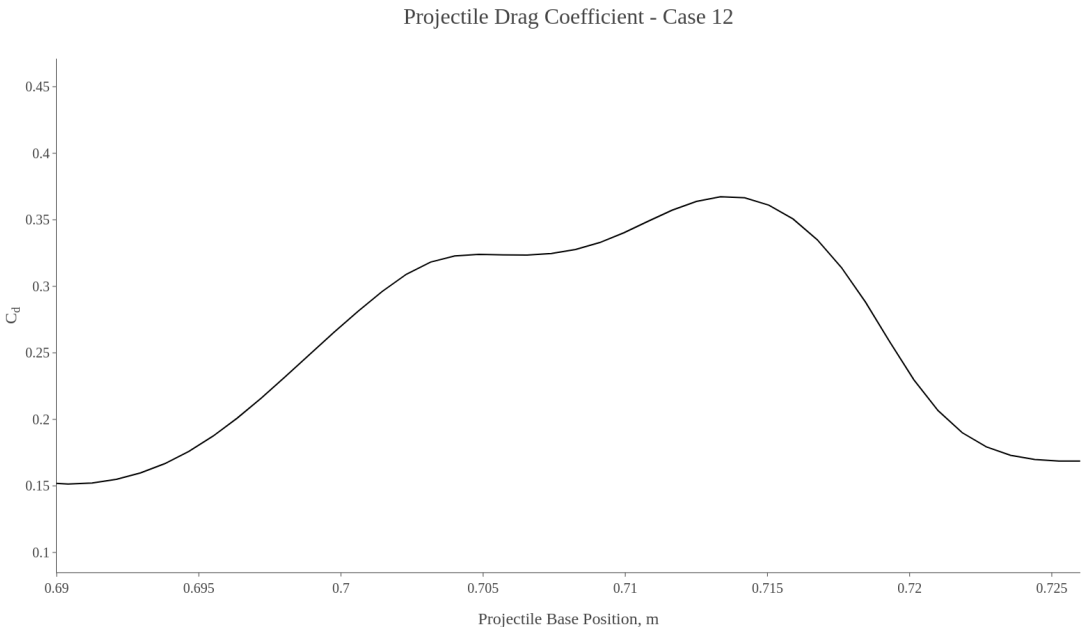

Figure 4.2: The drag coefficient as the projectile moves through one BTRA chamber.

the average, respectively.

Values for projectile C_d are shown in Figure 4.3 as a function of Mach number for the inviscid and turbulent simulations. The turbulent C_d values were approximately 3% higher than those from inviscid simulations, resulting from shear forces calculated in the turbulent cases. This is in line with Anderson [13] and the fact that supersonic drag is dominated by wave drag.

Oddly, C_d for the $M = 1.15$ case was lower than expected and does not follow the trend of the rest of the data or the typical behavior of drag coefficients with increasing Mach number. This un-physical behavior was not expected, and the cause has not yet been uncovered. It may be the result of a physics model setting in STAR-CCM+, a poorly posed boundary condition, or a bad choice of initial condition.

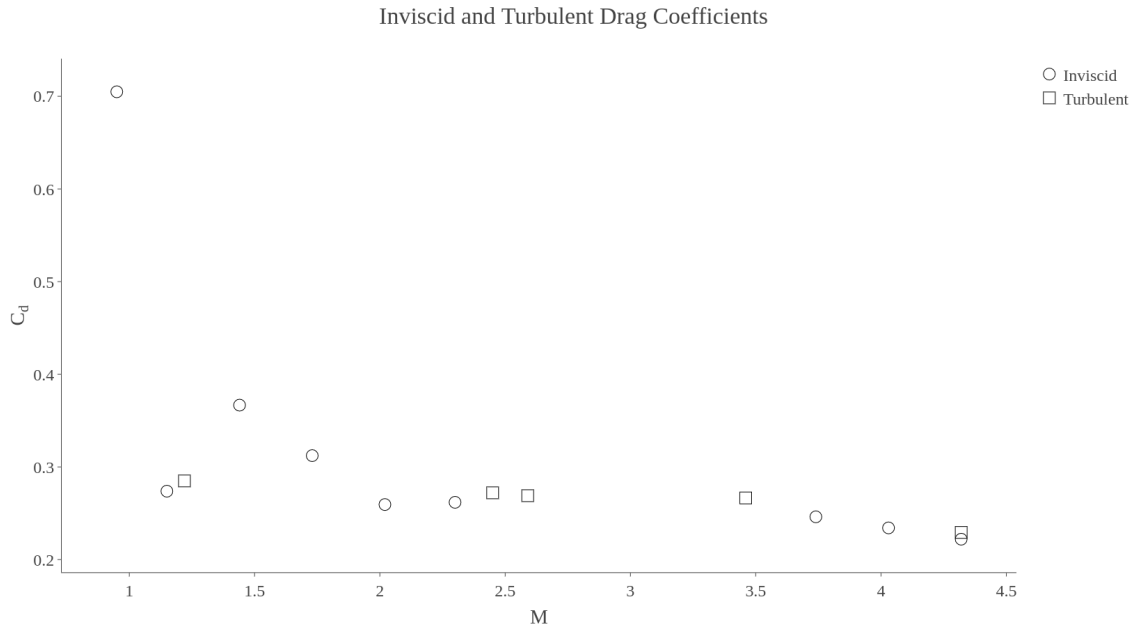

Figure 4.3: The projectile drag coefficient as a function of Mach number for inviscid and turbulent simulations.

4.1.2 Baffle Drag

Baffle drag was computed for cases 12-14,16, and 17. The number of chambers used in Equation 2.18 was $n_c = 6$, and the area used was the projected area of the baffles normal to the travel of the projectile. The cyclical nature of the drag coefficient as the projectile passed through the BTRA chambers is pictured in Figure 4.4, along with the moving average of the baffle drag coefficient.

4.2 Field Data

Aside from reports of drag forces on the projectile and baffles, data were recorded every 10 time-steps for the pressure, total pressure, density, total temperature, velocity magnitude, Mach number, and speed of sound fields in the computational domain, all in the lab reference frame. Some field data were used to monitor convergence of the solutions (i.e. was mass being conserved?), and some were used in calculating C_d values. Figures 4.6 and 4.7 illustrate sample field data from case 12.

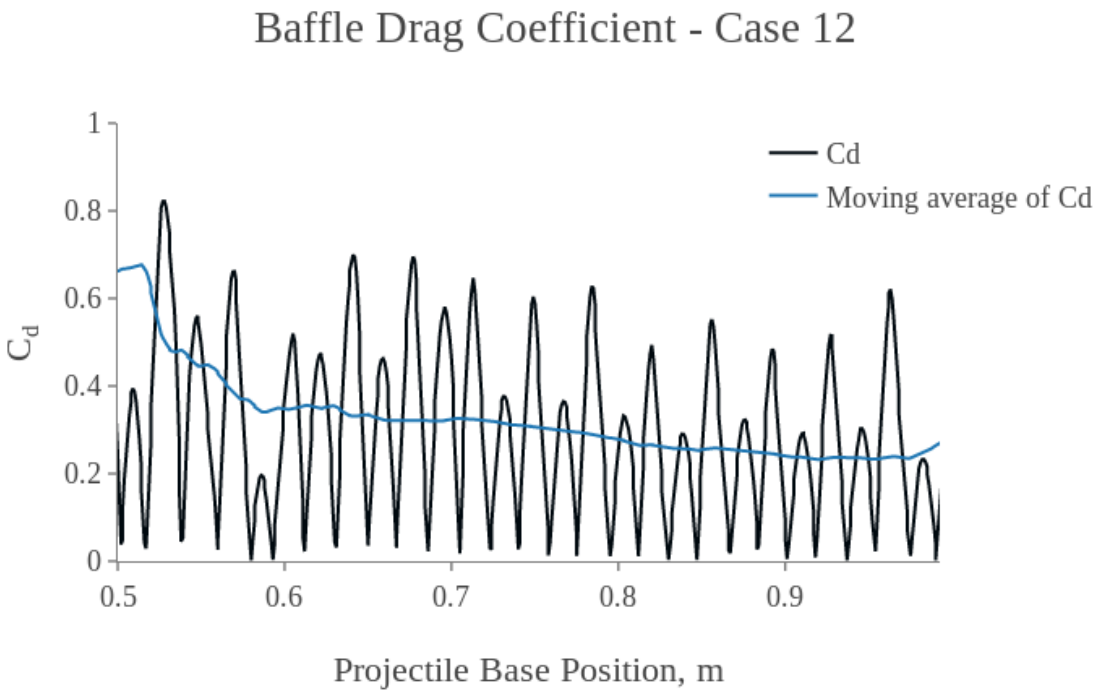

Figure 4.4: Baffle drag from case 12 (as a sample plot) with a moving average of the baffle drag. The window for the moving average corresponded to $n_c = 6$.

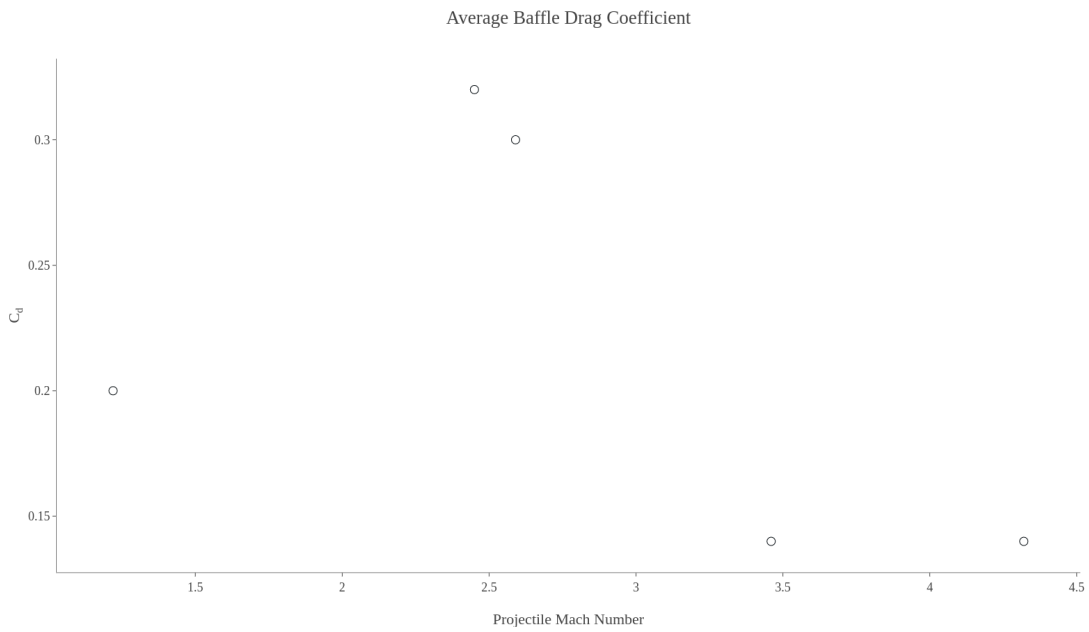

Figure 4.5: The average baffle C_d value for cases 12-14, 16, and 17.

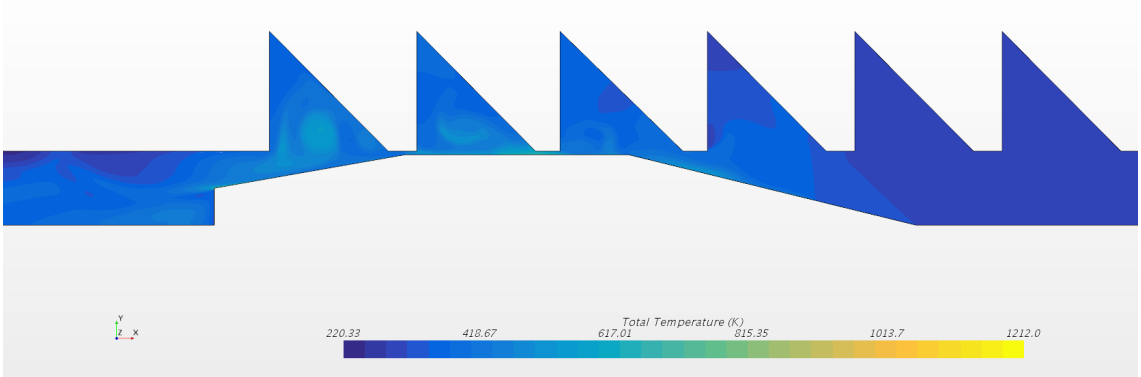

Figure 4.6: Example total temperature field data as the projectile passed through baffled-tube chambers.

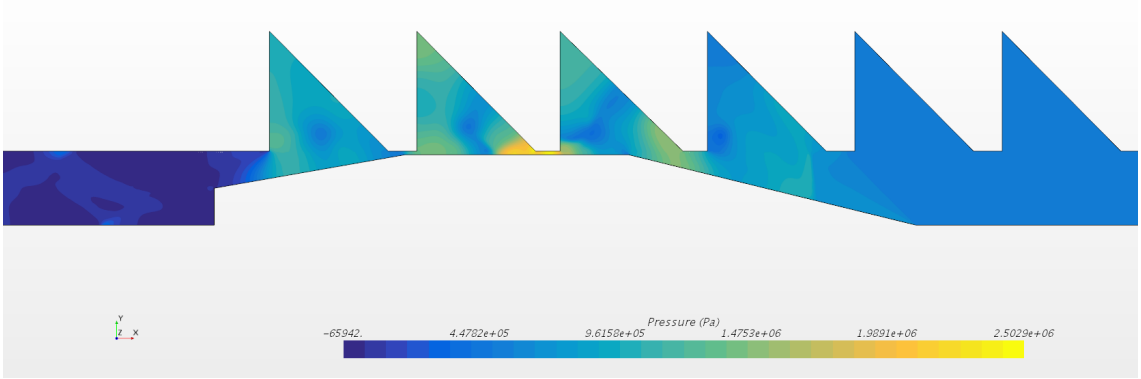

Figure 4.7: Example pressure field data as the projectile passed through baffled-tube chambers.

Table 4.1: Cold shot C96 experimental parameters and results.

d_{proj}, mm	m, g	P_{fill}, psig	v_{in}, m/s	v_{out}, m/s	Δv, m/s	M_{in}	M_{out}	I_{BTRA}
37.6	145	158	862.07	806.45	-55.62	2.47	2.31	-1.35

4.3 Comparison with Experiments

Table 4.1 outlines the parameters and results for the cold shot C96 experiment. The test used inert N_2 to fill the BTRA and the simulation from case 12 approximated the test conditions, with the main differences being baffle angle (45° for the computational domain vs. 30.8° for the test) and the constant Mach number of the simulation compared to the varying Mach number of the real BTRA.

4.4 Comparison with Previous CFD Work

The calculated values for C_d in my simulations were close to those previously determined using CFD [7, 8]. Discrepancies in the exact values were due, in part, to different computational geometries; both the projectile and baffle configurations were different. The meshes were also different, and the previous study included a roughness factor for the wall boundaries of the projectile and baffles.

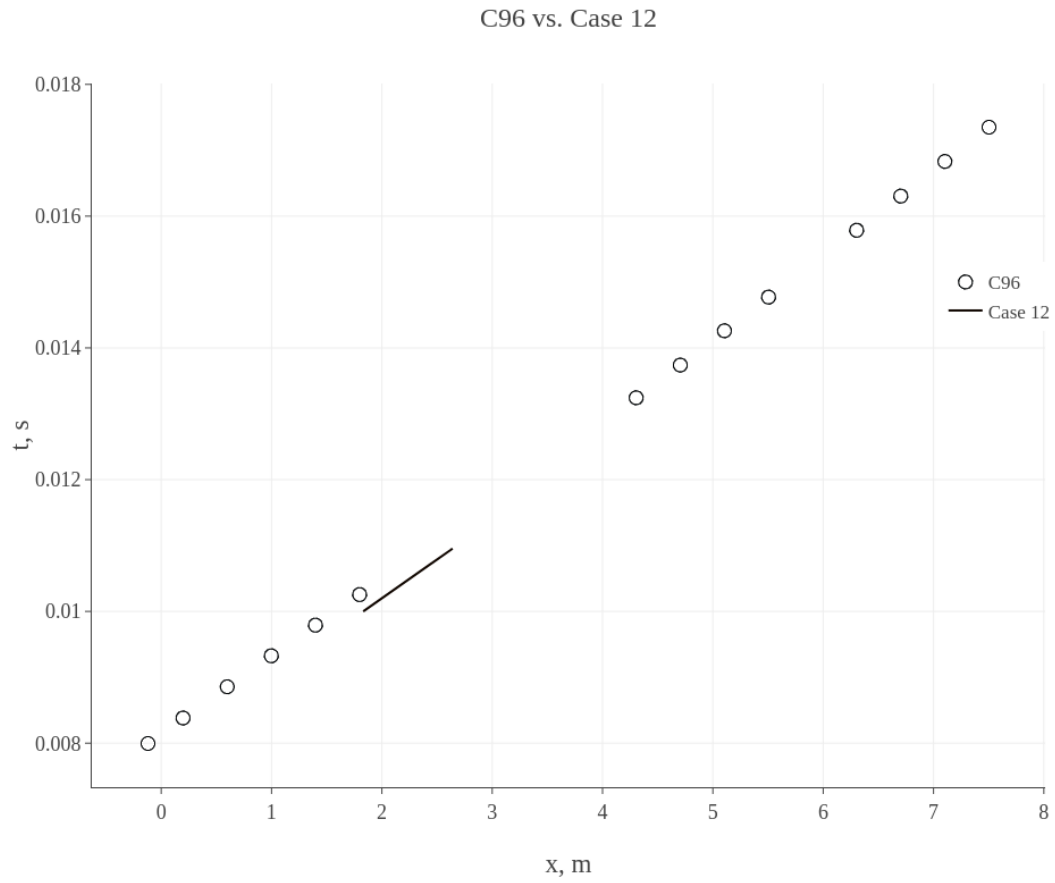

Figure 4.8: Time of flight data from cold shot C96 experiment and case 12 simulation. The data from case 12 was shifted in time and space to align the simulated projectile's flight through the baffled section with that of the real projectile in test C96.

Chapter 5

CONCLUSION AND FUTURE WORK

This research produced average C_d values for projectile and baffle drag. I consider the results good estimates, sufficient as part of an engineering tool, but lacking the rigor and uncertainty quantification of a deep scientific study. As with any research, I know there are many improvements that could be made to this study, and I have put together my thoughts on future work that could build on this in future theses or dissertations.

5.1 Optimization Studies

The current work could easily be used as part of optimization studies focused on minimizing projectile and baffle drag. STAR-CCM+ includes tools for optimizing geometries as a function of reports and monitors, and the methods I used to build the computational domain and mesh lend themselves to automated parametric sweeps of inputs like baffle and nosecone angle or particular lengths.

5.2 Mesh Refinement

The mesh in this study was fairly coarse (see section 3.4). Many simulations failed to converge because specific dissipation rate residual was larger than memory could handle. Mesh refinement could reduce this and other residuals and lead to more stable simulations. It would also be beneficial to show that the solution is mesh independent.

5.3 Accurate Geometry

Simulating the full 2 m BTRA test section (possibly as a three-dimensional wedge, rather than a two-dimensional axisymmetric domain) with 56 chambers would improve the estimates for the minimum entrance Mach number required to start. It would also be easier to compare with experimental data.

5.4 Reacting Flow

My simulations could be modified with additional physics models to study the reacting case, which is much better suited for comparison to experiments since the majority of experiments use combusting propellant mixtures. Simple chemical kinetic mechanisms have been implemented previously [7], but more advanced mechanisms could be used to accurately model the combustion process in the ram accelerator and capture the resulting impact on thrust and drag and the operating envelope of the baffled-tube ram accelerator.

BIBLIOGRAPHY

[1] Hertzberg, A., Bruckner, A., and Bogdanoff, D., "Ram accelerator-A new chemical method for accelerating projectilesto ultrahigh velocities," *AIAA journal*, Vol. 26, No. 2, 1988, pp. 195–203.

[2] Knowlen, C., *Theoretical and experimental investigation of the thermodynamics of the thermally choked ram accelerator*, Ph.D. thesis, University of Washington, 1991.

[3] Bruckner, A. and Hertzberg, A., "Ram Accelerator direct launch system for space cargo," 1987.

[4] Higgins, A., Knowlen, C., and Bruckner, A., "Ram accelerator operating limits, Part 1: identification of limits," *Journal of propulsion and power*, Vol. 14, No. 6, 1998, pp. 951–958.

[5] Knowlen, C., Glusman, J., Grist, R., Bruckner, A., and Higgins, A., "Experimental Investigation of a Baffled-Tube Ram Accelerator," *52nd AIAA/SAE/ASEE Joint Propulsion Conference*, 2016, p. 4813.

[6] Knowlen, C., Byrd, T., Dumas, J., Bruckner, A., and Higgins, A., "Baffled-Tube Ram Accelerator Operation with Inclined Baffles," *53rd AIAA/SAE/ASEE Joint Propulsion Conference*, 2017, pp. 49–59.

[7] Daneshvaran, N., *Transient computational fluid dynamic modeling of baffled tube ram accelerator*, Master's thesis, University of Washington, 2017.

[8] Daneshvaran, N. and Knowlen, C., "Transient computational fluid dynamic modeling of baffled tube ram accelerator," *55th AIAA Aerospace Sciences Meeting*, 2017, p. 0119.

[9] Knowlen, C., Daneshvaran, N., Byrd, T., and Dumas, J., "Computational Fluid Dynamic Modeling of Baffled Tube Ram Accelerator Experiments," *2018 AIAA Aerospace Sciences Meeting*, 2018, p. 1417.

[10] Glusman, J. F., *Theoretical Performance Model and Initial Experimentation of a Baffled-Tube Ram Accelerator*, Master's thesis, University of Washington, 2016.

[11] Knowlen, C., Bundy, C., Schwab, R., and Bruckner, A., "University of Washington, high pressure Ram accelerator facility," *50th meeting of the Aeroballistic Range Association (ARA), Pleasanton, California, USA*, 1999.

[12] Siemens Product Lifecycle Management Software Inc., *STAR-CCM+ User's Guide*.

[13] Anderson, J., *Modern Compressible Flow: With Historical Perspective*, McGraw-Hill series in aeronautical and aerospace engineering, McGraw-Hill, 1990.

[14] Spalart, P. R., "Strategies for turbulence modelling and simulations," *International Journal of Heat and Fluid Flow*, Vol. 21, No. 3, 2000, pp. 252–263.

[15] Bruckner, A., Knowlen, C., Hertzberg, A., and Bogdanoff, D., "Operational characteristics of the thermally choked ram accelerator," *Journal of Propulsion and Power*, Vol. 7, No. 5, 1991, pp. 828–836.

[16] Knowlen, C. and Bruckner, A. P., "Hugoniot analysis of the ram accelerator," *Shock Waves*, edited by K. Takayama, Springer Berlin Heidelberg, Berlin, Heidelberg, 1992, pp. 617–622.

Appendix A

SIMULATION DATA

To facilitate future work on the BTRA, I will host data extracted from this study's CFD simulations (for as long as I remember to maintain it) here: `https://jesdumas.github.io/thesisdata`